WASHINGTON STATE UNIVERSITY
Institute for Shock Physics

This paper is based upon work performed at the Dynamic Compression Sector, which is operated by Washington State University and sponsored by the U.S. Department of Energy (DOE) National Nuclear Security Administration. This research used resources of the Advanced Photon Source, a DOE Office of Science User Facility operated for the DOE Office of Science by Argonne National Laboratory.

Further Development of the Tamped Richtmyer-Meshkov Instability Method and Application to Molybdenum Dynamic Strength Calibration and Tabulation

T. J. Voorhees[1], A. Padgiotis[1,2], B. Zusmann[3,4], S. Guo[5], T. J. Vogler[1]

1 Sandia National Laboratories, Livermore, CA
2 Texas A&M University, College Station, TX
3 Georgia Institute of Technology, Atlanta, GA
4 Los Alamos National Laboratory, Los Alamos, NM
5 Sandia National Laboratories, Albuquerque, NM

DOI: 10.1007/s40870-025-00485-7

Published: October 2025

Journal of Dynamic Behavior of Materials

Journal of Dynamic Behavior of Materials
https://doi.org/10.1007/s40870-025-00485-7

RESEARCH PAPER

Further Development of the Tamped Richtmyer-Meshkov Instability Method and Application to Molybdenum Dynamic Strength Calibration and Tabulation

T. J. Voorhees[1] · A. Padgiotis[1,2] · B. Zusmann[3,4] · S. Guo[5] · T. J. Vogler[1]

Received: 29 April 2025 / Accepted: 19 July 2025

Abstract

The high pressure and high strain rate dynamic strength of Mo is experimentally and computationally investigated in the 3–20 GPa stress, 50–600 C temperature, and 10^5–10^6 /s strain rate regimes using a modified tamped Richtmyer-Meshkov instability (RMI) method. Modifications to the tamped RMI method include a method to determine loading states during strain, a new strength calibration function based on interface shape, and a robust uncertainty quantification method. These modifications improve fidelity of the tamped RMI method, allowing evaluation of the compensating effects of pressure hardening, strain rate hardening, strain hardening, and thermal softening. The new calibration function based on interface shape is not limited to sinusoidal corrugations and could be applied to additional interface shapes. Plate impact experiments are performed at Argonne National Laboratory's Advanced Photon Source's Dynamic Compression Sector operated by Washington State University (DCS), driving a planar shock front through a corrugated Mo-D_2O or Mo-C_8F_{18} interface, forcing the corrugation to significantly deform. The extent of interfacial deformation, RMI growth, is experimentally observed using X-ray phase contrast imaging at the DCS. RMI jet lengths and jet shapes are extracted from the experimental radiographs, then used to calibrate numerical simulations performed with the Sandia National Laboratories (SNL) hydrocode CTH. Mo yield strength, Y, as a function of shock pressure, P, strain rate, $\dot{\epsilon}$, accumulated strain, ϵ, relative volumetric compression, RD, and temperature, T, is determined for each impact experiment and presented. The calibrated Mo yield strength values range 1.2–1.8 GPa, with strength generally decreasing as the impact stress increases. This trend is likely caused by thermal softening or strain localization. The tabular yield strength versus loading condition data presented in this paper can be used to fit complex strength models.

Background

Strength is the ability of a material to sustain deviatoric stress. The magnitude of strength that a material exhibits is typically a function of the loading conditions at which plastic strain occurs: pressure, P, strain rate, $\dot{\epsilon}$, accumulated strain, ϵ, relative volumetric compression, RD, and temperature, T [1–4]. In dynamic deformation scenarios, such as shock compression or isentropic compression, the combined effects of pressure hardening, strain rate hardening, and thermal softening cause a material to exhibit significantly different strengths from what is observed in ambient conditions, e.g., quasistatic tensile tests. For example, ramp-release studies on Ta metal have shown nearly an order of magnitude increase in strength at 350 GPa pressure compared to near-ambient pressure [5]. Additionally, recent Richtmyer-Meshkov instability (RMI) studies on Cu metal have shown an approximately sixfold increase in strength from quasistatic (10^{-4} /s) to ultrahigh (10^7 /s) strain rates [6]. In contrast, shock induced thermal softening has been observed in shocked tin, leading to the complete loss of spall strength [7]. These hardening and softening effects have significant implications to the design of systems intended for extreme environments, such as ballistic armors, space vehicles, and

A. Padgiotis and T. J. Vogler and T. J. Voorhees are members of SEM.

✉ T. J. Voorhees
tjvoorh@sandia.gov

1 Sandia National Laboratories, Livermore, CA, USA
2 Texas A&M University, College Station, TX, USA
3 Georgia Institute of Technology, Atlanta, GA, USA
4 Los Alamos National Laboratory, Los Alamos, NM, USA
5 Sandia National Laboratories, Albuquerque, NM, USA

Published online: 13 October 2025

mining equipment. In this work, the dynamic strength and associated loading states of Mo metal are measured using the tamped Richtmyer-Meshkov instability (RMI) method and evaluated to understand the combined effects of pressure hardening, thermal softening, strain rate hardening, and strain hardening in the 3–20 GPa stress, 50–600 C temperature, 10^5–10^6 /s strain rate, and up to 24% strain regimes, respectively.

A variety of experimental methods can be used to explore the contributions of various loading conditions to dynamic material strength. Reviews of common experimental techniques for dynamic strength measurements are available in [8] and [9]. For strain rates beyond 10^5 /s, interfacial instabilities such as RMI have been used to infer material strength [10–17]. The RMI is characterized by shock compression loading of a nonplanar interface in the direction normal to the interface. A comprehensive review of RMI is presented in [18, 19]. A variety of experimental configurations exist that utilize RMI to probe material strength; of particular interest in this study is the tamped RMI method.

The Tamped RMI Method

The tamped RMI method probes material strength at a specific loading state by inducing plastic strain at an isolated region of pressure, temperature, and strain rate [20]. This method was first developed by Hudspeth, Olles, and Vogler and used to study the dynamic strengths of Cu metal and granular SiO_2 [13, 14]. A diagram of the specific tamped RMI configuration used in this work is shown in Fig. 1. In this configuration, two materials of disparate densities are placed in direct contact, forming a corrugated interface, then shock compressed. As in previous tamped RMI studies, the shock compression wave in this study is generated via planar impact. The two materials composing the target are referred to as the driver and tamper, with the driver material being the impacted and first shock compressed material. As the shock compression wave transmits through the driver-tamper interface and into the tamper, it generates significant vorticity. This vorticity induces significant deformation and, under certain conditions, the corrugated interface can invert to form a jet. Previous tamped RMI studies have primarily used RMI jet length as the main experimental measurement and strength model calibrant [13, 14].

Vogler and Hudspeth performed numerical sensitivity studies to investigate which experimental and material parameters govern the growth and evolution of RMI jets in impact-driven tamped RMI experiments [20]. The study concluded that the length of RMI jets is primarily controlled by five factors: the sum of the driver and tamper strengths, the Atwood number (A), the loading stress, and the initial corrugation aspect ratio ($k\eta_0$ for sinewaves). The values of A and $k\eta_0$ are defined by the equations:

$$\mathrm{A} = \frac{\rho_T - \rho_D}{\rho_T + \rho_D}$$

$$k\eta_0 = \frac{2\pi k}{\lambda}$$

where, ρ_T, ρ_D, k, η_0, and λ denote the tamper density, driver density, sinewave amplitude, wave number, and sinewave amplitude, respectively. Of these five factors, the loading stress, A, and $k\eta_0$ should be known measurable quantities defined by chosen material densities, component geometries, and impact conditions. The only unknown variables governing RMI growth should be the material strengths of the driver and tamper. To determine this combined strength of the driver and tamper, numerical simulations of the shock compression event can be iteratively performed with modulated strength model parameters until the experimentally observed RMI growth is reproduced. If the strength of one

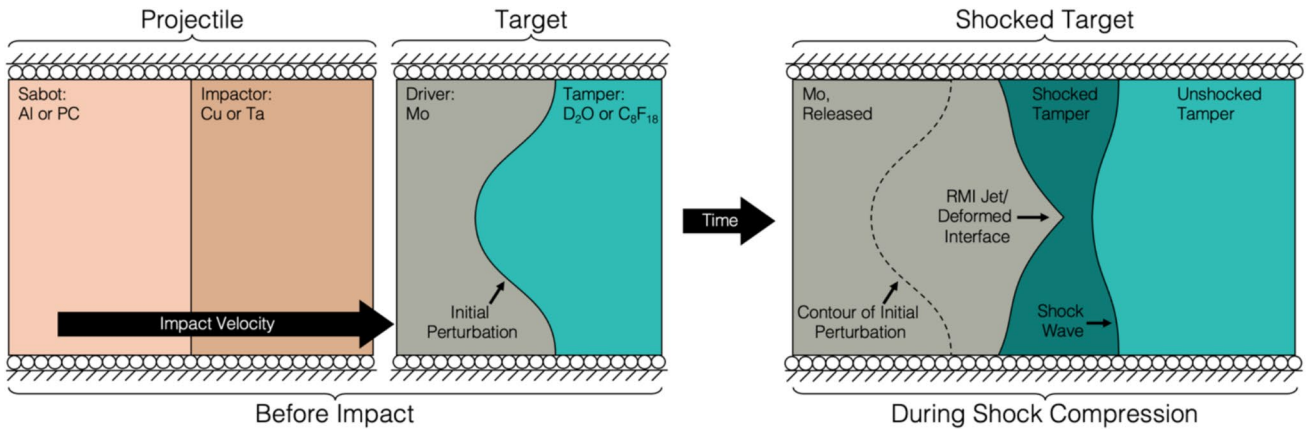

Fig. 1 Diagram of the tamped RMI experimental configuration used in this study

material is well-known or negligible, as in the case of a liquid, then the strength of the unknown material can be isolated. Tamped RMI experiments can be performed with a broad range of geometries and configurations, as described in [20]. In this work, the negative Atwood configuration is used in which the driver has a higher density than the tamper. Heavy water (D_2O) and perfluorooctane (C_8F_{18}) are used as liquid tampers, with A values of -0.80 or -0.70, respectively. The geometries of the driver-tamper interface corrugations tested in this study are sinusoidal with a constant 1.0 mm wavelength and varied amplitudes, with $k\eta_0$ values ranging 0.236–1.367.

In this work, three developments of the tamped RMI method are employed: (1) an alternative calibration method that uses the full contour of the driver-tamper interface as its calibrant, (2) an alternative method to determine the loading state (pressure, temperature, strain rate, plastic strain, and volumetric compression) associated with the calibrated strength values, and (3) a robust uncertainty quantification method to determine the uncertainty in calibrated strength values. These method modifications are discussed in depth in Sects. "Strength Calibration: Contour Comparison", "Loading State Determination", and "Uncertainty Quantification", respectively.

Previous Investigations of Molybdenum Strength

The strength behavior of Mo has been previously studied under quasistatic loading, impulsive/ramp loading, dynamic tensile fracture (spall) testing, uniaxial-strain shock compression loading, and oblique impact. The reported yield strengths, methodologies, and impact conditions from various studies are shown in Table 1. Many studies report dynamic yield strengths inferred from the Hugoniot elastic limit (HEL), reflecting some estimate of the stress that Mo can support prior to plastic deformation. The investigations by Steinberg [21, 22] and Alexander et al. [23], reported fitting parameters for the Steinberg–Guinan-Lund strength model, so the initial, Y_0, and maximum, Y_{max}, strength values are reported for these studies.

As shown in Table 1, the dynamic yield strength of Mo has been reported in various studies with values ranging 1.1 to 1.8 GPa. For many of the studies listed, a drive stress or peak stress state is reported. However, these reported stress states are often not the pressure that should be associated with the reported yield strength. For example, dynamic yield strengths inferred from the HEL measurements should be correlated with the elastic stress in the material. Additionally, the $\dot{\epsilon}$, ϵ, η, and T loading states that would be associated with the reported strengths are typically not reported.

Table 1 Reported dynamic yield strengths from experiments on Mo

Reported Y (GPa)	Methodology	Drive Conditions	Reference
1.8	Uniaxial plate impact, inferred from HEL	10–20 GPa	Chhabildas [24]
1.4	Shock and release	6–15 GPa	Furnish [25]
1.3	Uniaxial plate impact, inferred from HEL	6–15 GPa	Furnish etal., [26]
1.6	Uniaxial plate impact, inferred from HEL	7–15 GPa	Duffy &Ahrens, [27]
0.8–0.9	Heated uniaxial plate impact, inferred from HEL	12–31 GPa, 1400 C	Duffy &Ahrens, [27]
Y_0=1.6, Y_{max}=2.8	Fit to lower strain rate data, e.g., Hopkinson bar, then validated against plate impact experiments	–	Steinberg [21]
1.7	Uniaxial plate impact with lateral stress gauge	8–16 GPa	Cotton et al., [28]
Y_0=1.1, Y_{max}=2.8	Electromagnetically applied compression-shear ramp loading	–	Alexander etal., [23]
1.1	Symmetric oblique impact combined with numerical simulation	3–19 GPa	Johnson [1]
1.4–1.7	Symmetric oblique and uniaxial plate impact, inferred from HEL	3–19 GPa	Johnson, [1]

Without these loading states, it is difficult to make comparisons between these reported strengths and the strengths calibrated in the present study. The lack of loading state information also makes it difficult to calibrate complex strength models to these data.

In contrast, the studies by Steinberg, [21, 22] and Alexander [23] report fitting parameters for the Steinberg–Guinan-Lund (SGL) strength model and a modified version of the SGL model, respectively. The parameters reported by Steinberg, [21, 22] are used for comparison to the experimental data in Sect. "Comparison of EPP Model Fits to Steinberg–Guinan-Lund Model", and generally suggest that Mo is less strong than their reported model predicts.

Dynamic tensile fracture (spall) testing of Mo has been performed separately by Cotton and coworkers, Kanel and coworkers, and Chhabildas and coworkers, producing significantly different results [24, 28, 29]. The experiments by Cotton and coworkers showed low spall strengths near 0.7 GPa at 7 GPa stress, with the Mo spall strength decreasing to near zero as impact stress was increased [28]. The experiments by Chhabildas and coworkers found moderate spall strengths for Mo, near 2.3 GPa [24]. The experiments by Kanel and coworkers, which used single crystal Mo, reported high spall strengths, ranging from 3 to more than 10 GPa [29]. For ductile materials, spall strength is often correlated with material dynamic strength. However, for brittle materials spall strength can be more closely related to fracture behavior. The spall strength study by Chhabildas and coworkers included additional refractory metals and found no symmetric relationship between spall strength and yield strength, but did find a direct correlation between density-normalized spall strength and fracture toughness [24]. The large range in reported Mo spall strengths suggests that the brittle nature of Mo could lead to damage during RMI experiments if tensile loading states are significant. To avoid the effects of damage, the current study uses liquid tamping to reduce release and thus reduce the potential of rupturing at the RMI bubble locations. The current study also limits the temporal region of interest to remove the hazardous effects of release waves, as discussed in Sect. "Temporal Region of Interest for Model Calibration".

In the lower strain rate regime, Scapin and coworkers studied the strength of high purity Mo samples from two vendors, Plansee and AT&M, varying strain rates 10^{-3} to 10^{3} /s at ambient temperature, then varying the temperature from ambient to 1000 C at either 10^{-3} or 10^{3} /s strain rates [30]. Scapin and coworkers describe the strain hardening, strain rate hardening, and thermal softening behaviors of Mo within these strain rate regimes, noting that the strain-induced adiabatic heating observed in the 10^{3} /s experiments could cause an overall softening effect, such that thermal softening had a greater contribution to material strength than strain and strain rate hardening combined [30]. We find similar results regarding the compensating behaviors of thermal softening and strain rate hardening in the current study.

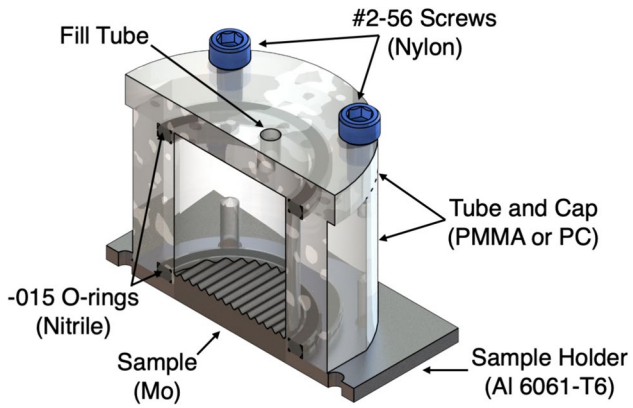

Fig. 2 Half-section diagram of the target design used in this study

Table 2 Nominal dimensions of the target assembly components

Component	Material	Inner Diameter (mm)	Outer Diameter (mm)	Thickness (mm)
Sample	Mo	–	13.5	2.9
Tube	PMMA or PC	13.5	25.4	25.4
Cap	PMMA or PC	–	25.4	3.2

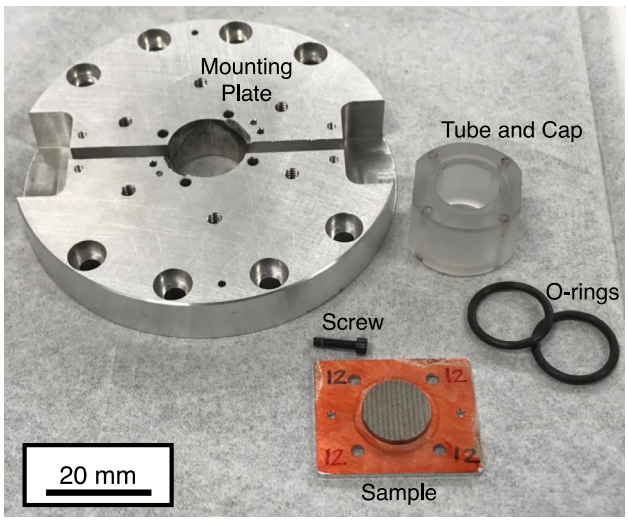

Fig. 3 Photograph of selected target components

Experimental Setup

Tamped RMI experiments are performed at the Argonne National Laboratory's (ANL) Advanced Photon Source's (APS) Sector 35: Dynamic Compression Sector (DCS) operated by Washington State University. These experiments use the single stage gas gun (SSGG) or powder guns (PG) to impact the target assembly with 10 mm diameter copper and tantalum flyer plates. The 10 mm flyer plate diameter defines the main design constraint for the present study. Target assemblies are designed to hold a Mo sample with a corrugated surface in direct contact with D_2O or C_8F_{18}, as shown in Fig. 2. The Mo sample is press fit into an aluminum target holder, which is fastened to a clear plastic tube and cap. The surfaces between the aluminum target holder, tube, and cap are sealed with O-rings. The tamper fluid is injected into the cell through the fill tube, which is then plugged with a sealing screw. Nominal dimensions of the main sample components are presented in Table 2 (Fig. 3).

In this design, a Mo disk is press fit into an aluminum sample holder. This sample holder is machined with 4 through holes and 2 dowel pin holes. The dowel pin holes are used for alignment, both during machining and during impact experiments at DCS. During machining, the sinewave profile is machined into the Mo surface via wire electronic discharge machining (EDM), aligning the sample's dowel pin holes to be perpendicular to the EDM wire. To reduce thickness of the EDM recast layer, the profile is machined in 5 passes. During impact experiments at DCS, the target assembly is rotationally aligned via mating dowel pin holes in the mounting plate. A slightly modified version of the standard DCS target mounting plate design [31] is used: counterbored holes are machined into the uprange face of the mounting plate that match the four holes in the sample holder and plastic tube. Screws fasten the mounting plate, sample holder, and tube together, crushing an O-ring in the gland between the sample holder and tube. This pass-through fastener design reduces the potential for buckling or warping of the thin aluminum sample holder that would occur if screws were fastened directly to its surface. Similarly, screws fasten the cap to the tube with an O-ring crushed in the gland between. The resulting chamber holds the tamping fluid, D_2O or C_8F_{18}, which is injected through the fill tube with a plastic syringe. After filling the chamber with tamping fluid, a sealing screw is fastened into the fill tube to ensure the cell is hermetically sealed. The assembled target is mounted to the muzzle of the DCS guns.

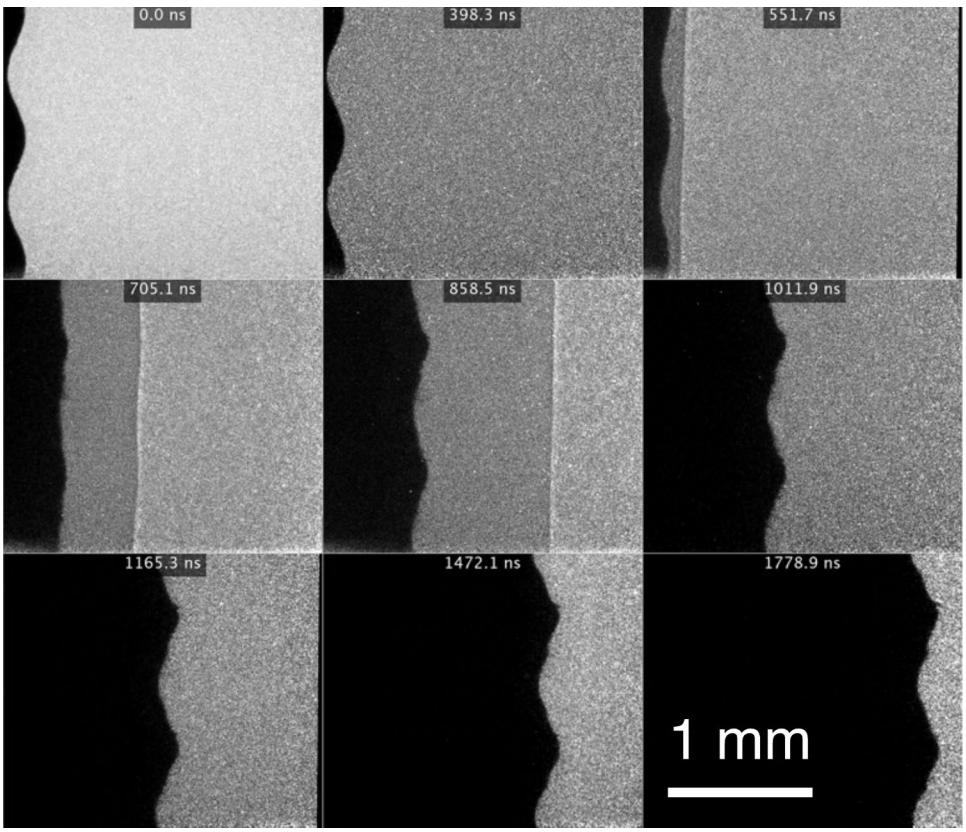

Fig. 4 Radiographs taken during the 22–4-035 experiment. Impact direction is shown as rightwards

Data Acquisition and Imaging Techniques

Impact experiments are performed using the DCS SSGG and PG to impact the uprange, flat face of the Mo sample with Cu or Ta flyer plates at impact velocities ranging 529 to 2390 m/s. Up to eight in situ phase contrast radiographic images of the Mo-tamper interface are taken at 153.4, 306.8, or 613.6 ns intervals using X-ray radiation from the ANL APS synchrotron (23–26 keV X-ray, U17.2 undulator) as the light source and the DCS imaging system to record contrast images. A full description of the DCS imaging system is available in [32]. In this study, the 5X magnifying optic is used, resulting in a 2.50 μm/pixel resolution and an approximately 2.2×2.5 mm^2 field of view. In all experiments, a 15 mm undulator gap is used and all images are aligned to the radial center of the gun barrel, i.e., the radial center of the flyer plate. This alignment definition is chosen because the sample's radius is larger than the flyer plate, thus choosing to align to the center of the gun barrel ensures that the imaged location experiences edge release at the latest time, even when the flyer and sample are not perfectly concentric. An example montage of radiographs taken during an impact experiment is shown in Fig. 4. The dark material is Mo and the light material is D_2O. Time labels are shown with respect to the triggering diagnostic, not the temporal frame of reference used in calibrations. Peak-to-peak distance along the sinusoidal interface is 1.00 mm.

Image Analysis and Data Extraction

Image Registration and Resolution Determination

Images are taken on four cameras, each with a different vantage. Image registration is thus performed on a per-camera basis so that all image data can be compared with the same spatial frame of reference. To perform this process a dot grid with 100 μm spacing is imaged through the X-ray beam with all four cameras. Image analysis is performed using MATLAB, version R2020b. Image rotation and translation is performed using the imregtform function. Image resolution determination is performed using the imfindcircles function to fit circles to each dot in the grid, then extract the Euclidean center-to-center distance between each neighboring set of dots. The pixel resolution across all experimental series was found to be 2.5000 ± 0.0008 μm/pixel.

Image Flatfielding

Flatfielding is used to improve image contrast, thus reducing uncertainty in extracted contour locations. The flatfielding process normalizes images by the maximum and minimum intensity that the cameras could record. These values are determined by taking 20 whitefield and 20 darkfield images on each camera immediately before each experiment. Whitefield images are taken by removing the sample from the field of view and recording images with the X-ray beam present, representing the maximum intensity the camera could record after the X-ray beam has transmitted through the windows of the gun chamber and imaging optics. Darkfield images are taken when the X-ray beam is not present, representing image intensity for zero transmission. Flatfielding is performed on a per-camera basis, subtracting the darkfield images, then dividing the remaining image intensity by the difference of the whitefield and darkfield images.

Extraction of Driver-Tamper Interface Contours

The location of the interface between the Mo and tamping fluid is extracted from each flatfielded image through a combination of masking, thresholding, and edge finding methods in MATLAB. First, a polygonal region of interest is hand-selected around the interface, typically at a 20–50 pixel standoff distance, defining a mask. Then, a 20 pixel length median filter (blur) is applied to the image. The blurred image is then converted to a logical array via thresholding, with the threshold applied at 5%, 6% or 10% of maximum flatfielded intensity for images showing D_2O tampers, D_2O tampers with visible O-rings, and C_8F_{18} tampers, respectively. Threshold values were determined empirically by iteratively overlaying the extracted edge with the original image until the best match was found. The edge of the logical threshold image is determined via Canny edge detection and restricted to values only within the previously defined

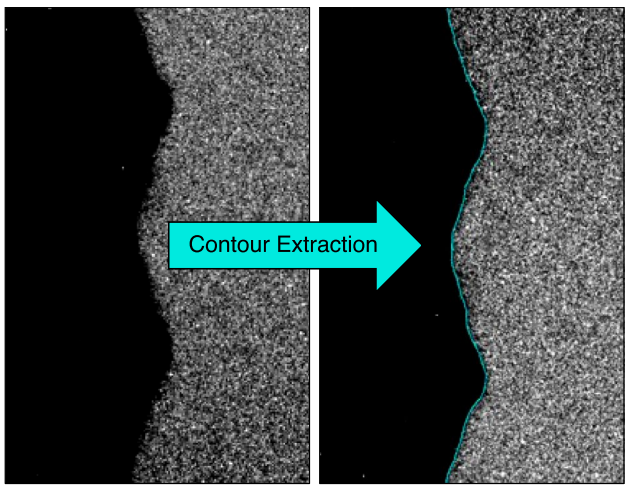

Fig. 5 Contours are extracted from the phase contrast images: (left) the original image is shown on the left, (right) the extracted contour is overlaid as a cyan line. Impact direction is shown as rightwards

mask. The extracted edge is then used for comparison to simulations and jet length extraction. An example radiograph with extracted contour overlaid is shown in Fig. 5.

Jet lengths are extracted from the interfacial edge location data by determining the location of the central bubble and two neighboring spikes. The jet length is calculated for each image as the Euclidean distance between the central bubble and the midpoint of the two spikes.

Rotational Alignment of Interface Contours

The interfacial contours must be rigidly translated and rotated to align with and be compared to simulation data. This alignment is performed by finding the translation and rotation parameters which cause the two imaged RMI jets to be perfectly mirrored across the central bubble. To perform this alignment optimization, driver-tamper interfacial contours are translated such that the central bubble is the origin, then rotated and chopped into two point clouds: positive and negative with respect to the central bubble location. The negative point cloud is mirrored across the central bubble and the average distance between the positive and negative point clouds is calculated. This process is iterated with varied translation and rotation values until the global minimum is found. This global minimum is defined as the ideal rotation and translation and is then applied to all contours for the given experiment. Once this process is completed, the negative and positive point clouds are combined into the final contour point cloud, so that simulations are calibrated to both sides of the sinewave. This process is repeated for each image of each experiment.

Uncertainty Quantification for Radiography: Edge Reproduction

The systematic uncertainty associated with how interfacial contour locations are extracted from radiographs is determined by evaluating the spread in extracted contour locations from pre-shot static images. Prior to each experiment, 20 white field, 20 dark field, 20 ambient, and 2 pre-shot test trigger images are taken on each camera. This results in a total of 88 flatfielded pre-shot static images per experiment. To calculate the spread in contour location as a function of processing method, each of these 88 images are pushed through the same extraction method described in the preceding subsection. This generates 88 pre-shot contours per experiment. The spread in these 88 contours is determined as the spread from the camera-specific average contour location along 1 central wavelength, using a 2.5 μm (1 pixel) bin size. This spread is calculated for each contour position (singular pixel) of the 88 extracted contours and calculated as the minimum Euclidean distance from the extracted contour location to the average contour. This process generates 40,000–60,000 deviation distances per experiment, with the number of deviation distances being dependent on the arc length of the imaged sinewave. A histogram of deviation distances for shot 22–4-035 is shown in Fig. 6.

These histograms define the systematic uncertainty in RMI contour location, which is a critical component of the overall experimental uncertainty. From this histogram, the standard deviation is defined as the 68.27% confidence interval. This standard deviation is calculated for each experiment and reported as the edge reproduction uncertainty, δ_{ERU}, in Table 7.

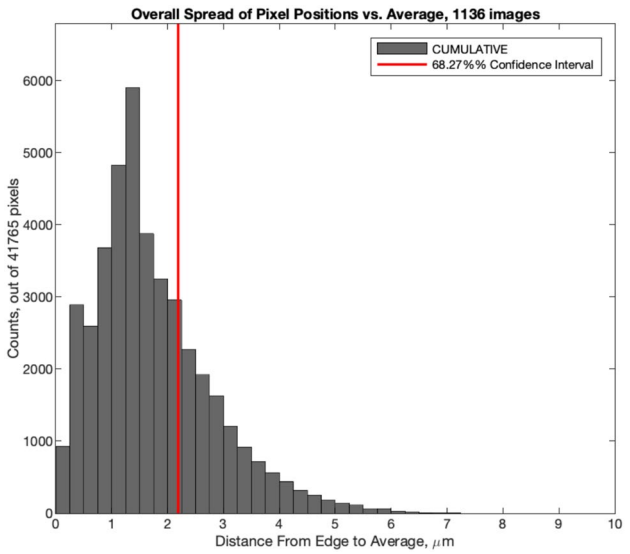

Fig. 6 Histogram of pixel deviation distances for experiment 22–4-035 with 68.27% confidence interval plotted, which is used to define the standard deviation

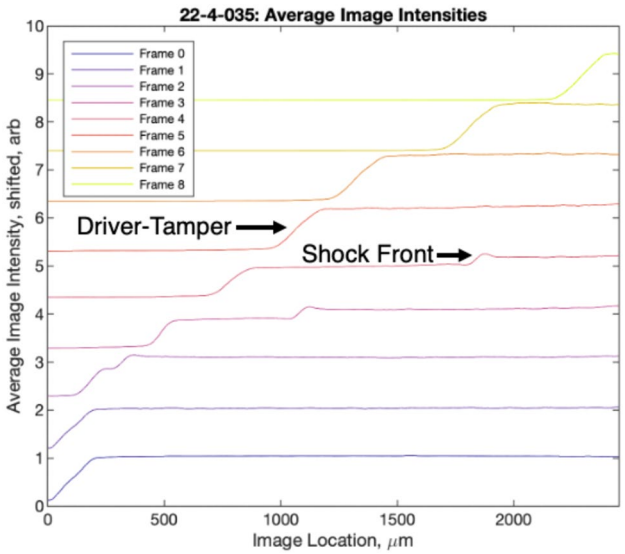

Fig. 7 Average image intensity in the impact direction for shot 22–4-035.y

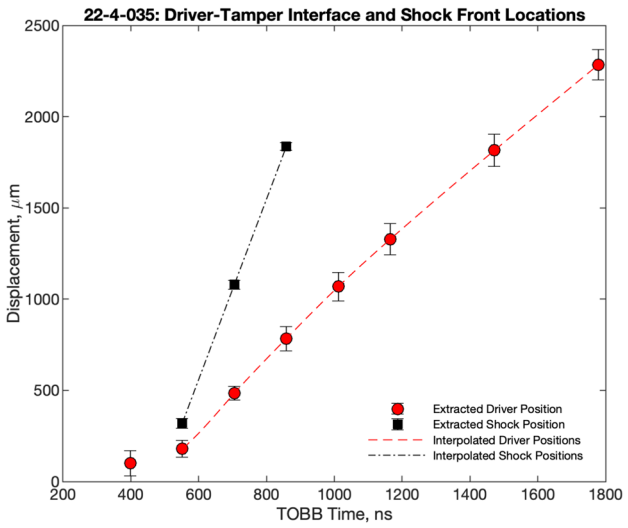

Fig. 8 Extracted mean driver-tamper interface and shock front positions for shot 22–4-035. Time is shown with respect to the triggering diagnostic

Edge reproduction uncertainty values are generally small across the range of experiments, ranging from 2.19 to 3.83 μm across the series of experiments.

Time of Shock Entry Determination

Time of shock entry is extracted from the phase contrast images by tracking the driver-tamper interface and shock front locations, then fitting a spline function to these positions as a function of time and extrapolating to the time where the shock front and driver-tamper interface coincide with the pre-shot driver-tamper interface location. This process is performed by calculating the average image intensity in the impact direction along 2 wavelengths, i.e., mean intensity per column of pixels, then extracting the location of significant intensity variations. A plot of average image intensities for shot 22–4-035 is shown in Fig. 7. The extracted driver and shock positions are shown in Fig. 8, note that the slopes of the driver position and shock position lines are descriptive of the particle and shock velocities, respectively.

The plots in Fig. 8 can be extrapolated in the negative time direction to determine the time when the average driver-tamper interface and shock front positions would meet the pre-shot driver-tamper interface location. This extrapolated time is defined as the time of shock entry and corresponds to when the shock front first reaches the mid-plane of the sinusoidal driver-tamper interface. This time is used as the reference time in later model calibration steps, as discussed in Sect. "Frame of Reference Determination".

Numerical Simulations Using CTH

Simulations are performed using the Sandia National Laboratories (SNL) hydrocode CTH [33] in 2D Cartesian geometry, capturing the behavior of the driver, tamper, flyer plate, and sabot. All other components were determined to cause negligible effects on RMI evolution and are not included. Because of the small diameter of the flyer plate, the simulation extends from the radial center of the Mo driver to just beyond its outer radius, 6.75 mm. This allows edge release to be simulated along one dimension. A mirror boundary is applied at the radial center of the Mo driver, while an outflow boundary is applied at a distance two mesh elements beyond its outer radius. The tamper is modeled with a 6.75 mm radius to match the Mo driver, and an infinite thickness extending beyond the downrange outflow boundary condition. The flyer plate is modeled with a 5 mm radius and a thickness that matches the experimentally measured value. The sabot is modeled with a matching 5 mm radius

Table 4 EPPVM strength model parameters applied to the simulated components

Component	Material	Y (GPa)	ν
Driver	Mo	Y*	0.29
Flyer	Cu	0.47	0.36
Flyer	Ta	0.75	0.33

Y* indicates that the Mo yield strength is varied in simulations.

Table 3 Mie-Grüneisen EOS models parameters applied to the simulated components

Component	Material	ρ_0 (g/cm^3)	C_0 (mm/μs)	S1	S2	$\gamma 0$	C_V ($\frac{J}{g*^\circ C}$)	Reference
Driver	Mo	10.210	5.03	1.265	–	1.490	0.249	[33]
Tamper	D_2O	1.110	1.48	1.984	–	0.480	3.689	[14]
Tamper	C_8F_{18}	1.770	0.86	1.886	–	0.480	3.689*	[35]
Flyer	Cu	8.930	3.94	1.489	–	1.990	0.393	[36]
Flyer	Ta	16.654	3.39	1.220	0.050	1.600	0.138	[35]
Sabot	Al6061-T6	2.703	5.22	1.370	–	1.970	0.922	[22]
Sabot	PC	1.186	2.30	1.750	−0.130	0.910	3.017	[35]

Value for water is applied

and an infinite thickness, extending beyond the uprange inflow boundary condition. An initial downrange-oriented velocity is applied to the sabot and flyer plate that matches the experimentally measured impact velocity, generating the shock compression event. A uniform mesh element length of 2.0 of 10.0 μm is applied depending on if simulations are run for strength model calibration or uncertainty quantification, respectively, which will be discussed in Sects. "Dynamic Yield Strength Calibration" and "Uncertainty Quantification".

All materials are modeled using a Mie-Grüneisen EOS and Elastic-Perfectly Plastic Von Mises Criterion (EPPVM) yield strength. The suitability of the EPPVM model to capture the average strength throughout the RMI growth and evolution event is being numerically verified and validated through a separate study that will be published in the near future [34]. The constitutive model parameters applied to the modeled components are presented in Tables 3 and 4. Melt temperatures are set to an effectively infinite value, 10 eV (115,767 °C), to ensure that thermal softening is not active for the EPPVM model. The sabot and tamper are modeled without strength models, as strength of the sabot has negligible effects on RMI evolution, and the liquid tamper is assumed to have negligible strength in comparison to the Mo metal. Fracture is assumed to not occur within the temporal region of interest and is not modeled.

Dynamic Yield Strength Calibration

The dynamic strength of Mo is determined by calibrating hydrocode simulations to the experimental radiograph data. The two calibrants investigated are the driver-tamper interfacial contour shape and jet length. The following subsections define the spatial and temporal frames of reference, temporal region of interest, and application of the contour calibration and jet length calibration processes.

Frame of Reference Determination

To directly compare experimental and simulated results, common spatial and temporal frames of reference must be defined. In this work, the spatial origin is defined as the radial center of the molybdenum-tamper interface, i.e., the central bubble. The temporal reference, t_0, is defined as the time at which the shock wave reaches the mid-plane of the sinusoidal molybdenum-tamper interface. In the experimental data, this time is determined by tracking the average position of the shock front and driver-tamper interface along two wavelengths (2.00 mm), as described in the preceding section. In the simulated data, this reference time is defined by pressure arrival at the sinusoidal interface's mid-plane, halfway between the sinewave's peaks and valleys.

The spatial origin is defined as the central bubble location in a Lagrangian format. By selecting the central bubble, the comparison focuses solely on interfacial deformation and removes the equation of state effect of interfacial

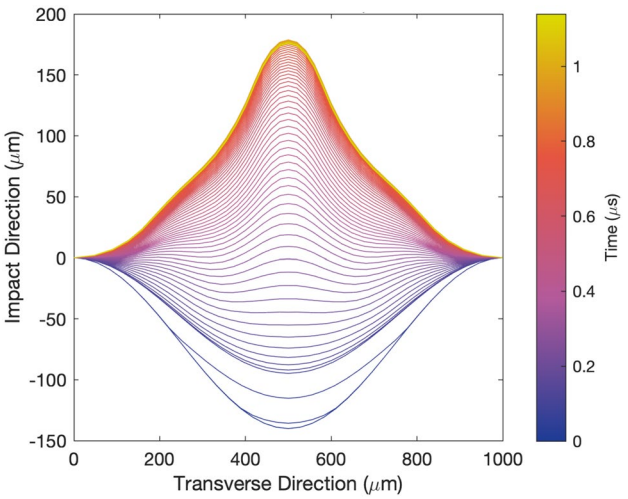

Fig. 9 Example of driver-tamper interfacial deformation (RMI evolution) using the central bubble as the dynamic spatial origin. Contours are colored by time, plotted at 0.010 μs intervals. Impact direction is shown as upwards

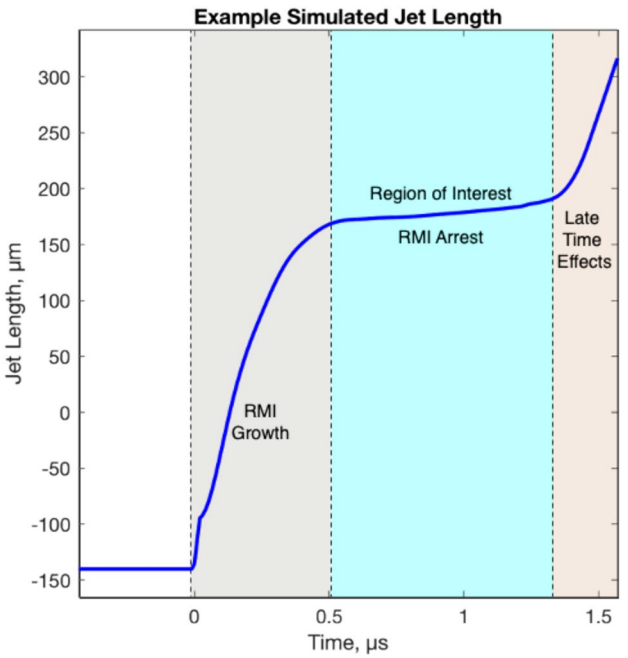

Fig. 10 Simulated jet length profile with labels for RMI growth, RMI arrest, and late time effects. The time axis is shown with respect to shock breakout, as discussed in Sect. "Frame of Reference Determination"

translation. The radial-axis is defined as the absolute value of distance from the origin, mirroring the sinewave profile across the impact direction-axis. This is chosen to improve rotational alignment of the experimental contour, defining contour rotation as the value where the pre-shot sinusoidal interface best aligns with itself, as previously described in Sect. "Rotational Alignment of Interface Contours". An example of simulated contour locations using this Lagrangian frame of reference is shown in Fig. 9 for shot 22–4-035.

Temporal Region of Interest for Model Calibration

Previous tamped RMI work has shown that the greatest sensitivity to material strength occurs after the RMI growth arrests. In this work, the temporal region of interest applied to model comparison is defined as the time period between RMI growth and the occurrence of late time effects caused by edge release, rarefaction, or shock reflections. This time period is visualized with a simulated jet length profile in Fig. 10.

Strength Calibration: Contour Comparison

The contour comparison method evaluates how well the computational model captures the experimentally observed deformation by quantitatively comparing the simulated driver-tamper interfacial contour to the experimentally measured interfacial contour. For this process, CTH simulations are performed with a 2.0 μm uniform mesh size (500 elements/wavelength) generating a total of 212.8 million cells within each calculation. Experimentally observed contours are extracted using the process in Sect. "Extraction of Driver-Tamper Interface Contours". Simulated interfacial contours are calculated using a set of 19 Lagrangian tracer points implemented at the driver-tamper interface with equal spacing along the central half wavelength of the simulation, i.e., central bubble to nearest spike. Simulated contours are translated to the dynamic frame of reference described in Sect. "Frame of Reference Determination" by subtracting the coordinates of the central bubble. To compare the simulated and experimental contours, the minimum Euclidean distance between each simulated point and the point cloud of experimental locations is calculated. The mean of these calculated distances is defined as the cost function for the contour calibration process. An example plot of mean contour distance vs. simulated yield strength is shown in Fig. 11 with overlaid plots of the experimental and simulated contour in Fig. 12. The minimum of a polynomial fit to the deviation distance curve defines the calibrated strength value for the experiment. This process is repeated for each experiment, and contour comparison calibrated yield strength values are reported in (Table 5) as $Y_{Contour}$.

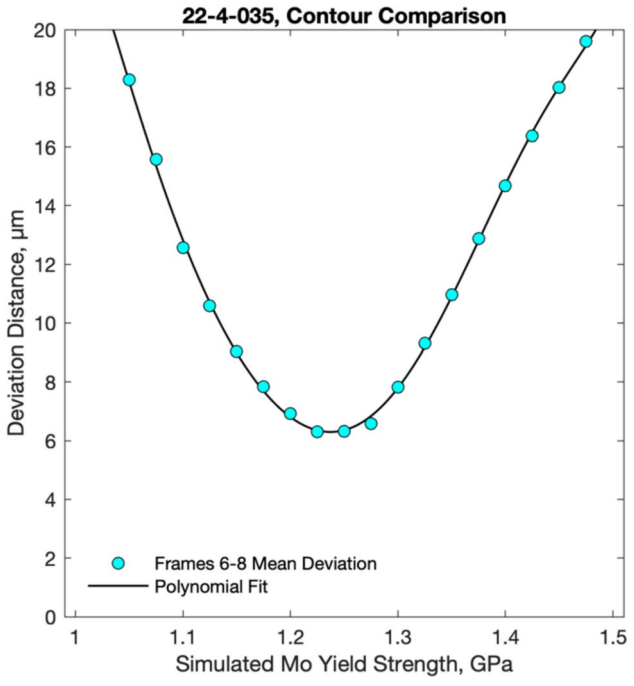

Fig. 11 Calibration curve for the contour comparison method applied to Shot 22–4-035. The mean deviation distance is plotted as a function of simulated Mo yield strength

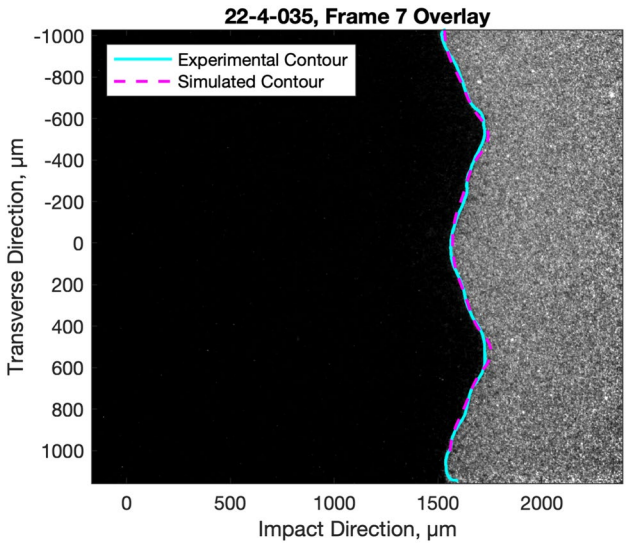

Fig. 12 Comparison of the simulated and experimental jet contours for frame 7 in Shot 22–4-035 overlaid on the experimental radiograph. The simulated yield strength in this figure is 1.225 GPa and mean contour deviation is 5.9 μm. Impact direction is shown as rightwards

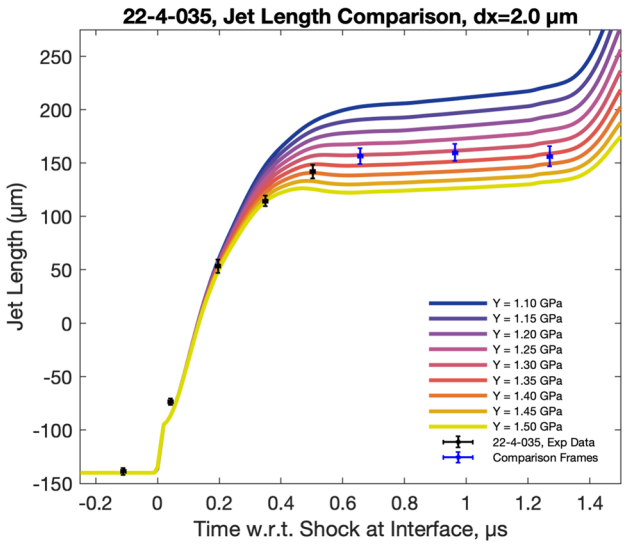

Fig. 13 Comparison of experimentally measured jet lengths with simulated jet lengths of varied yield strength for 22–4-035. The experimental data used for comparison with simulations is denoted as the 'Comparison Frames' and plotted in blue

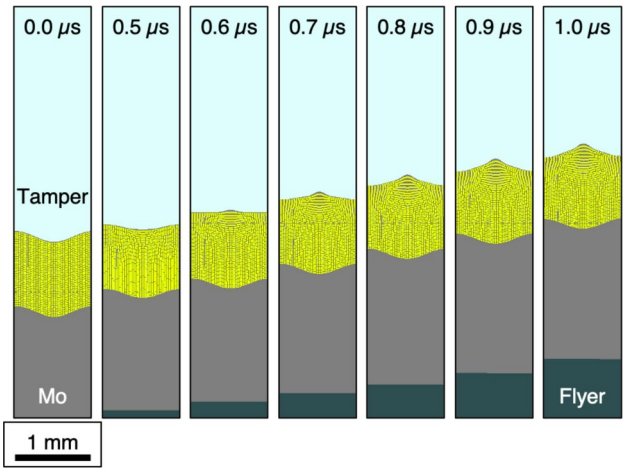

Fig. 14 For loading state determination, tracers are placed throughout the Mo driver with approximately equal 25 μm spacing. In this figure, tracers are plotted as yellow squares. Impact direction is shown as upwards

Strength Calibration: Jet Length Comparison

The jet length comparison method follows a similar methodology to that employed by Hudspeth and coworkers [13] and Olles and coworkers [14]. In this method, simulated jet lengths are extracted from the CTH simulations and compared to the experimentally measured values. A plot of simulated jet lengths vs. the experimentally measured values is shown in Fig. 13. The mean deviation in jet lengths across the temporal region of interest, as defined in Sect. "Temporal Region of Interest for Model Calibration", is calculated and used as the calibration cost function. Similar to the contour comparison method, the minimum of a polynomial fit to this mean deviation curve defines the calibrated strength value for the given experiment. Jet length calibrated yield strength values are reported in Table 5 as $Y_{JetLength}$.

Loading State Determination

Tamped RMI experiments induce strain at relatively precise loading conditions, i.e., pressure, temperature, and strain rate. To determine the loading conditions associated with each calibrated yield strength, histograms of the

Table 5 Calibrated yield strengths per experiment

SHOT ID	*Vel.* (km/s)	Impactor	Tamping Fluid	$k\eta_0$	$Y_{Contour}$(GPa)	$Y_{JetLength}$(GPa)	σ_{Drive}(GPa)	$\sigma_{Release}$(GPa)
22–4-024*	2.390	Cu	C_8F_{18}	0.236	–	–	70.04	14.52
22–4-025	1.049	Cu	D_2O	0.660	1.720	1.708	25.86	2.90
22–4-026	1.404	Cu	C_8F_{18}	0.660	1.670	1.782	36.37	5.80
22–4-027	1.456	Cu	D_2O	0.660	1.446	1.652	37.98	4.81
22–4-028	1.854	Cu	C_8F_{18}	0.660	1.484	1.598	50.93	9.33
22–4-029	2.277	Ta	D_2O	0.440	1.211	1.276	82.65	13.46
22–4-030	2.223	Ta	C_8F_{18}	0.440	1.405	1.452	80.19	17.46
22–4-035	2.066	Ta	D_2O	0.440	1.234	1.282	73.17	11.47
22–4-036	2.326	Ta	C_8F_{18}	0.440	1.311	1.329	84.91	18.56
23–2-006	0.769	Ta	D_2O	1.367	1.374	1.481	23.04	2.49
23–2-007	0.529	Ta	D_2O	1.367	1.491	1.262	15.32	1.47
23–1-005*	1.344	Cu	D_2O	1.367	–	–	34.53	4.24
23–1-006*	1.459	Cu	D_2O	1.367	–	–	38.08	4.83

Drive and release stresses, σ_{Drive} and $\sigma_{Release}$, are calculated via impedance matching. *Vel* indicates impact velocity. Shots marked with asterisks do not show calibrated strength values because fracture may have occurred

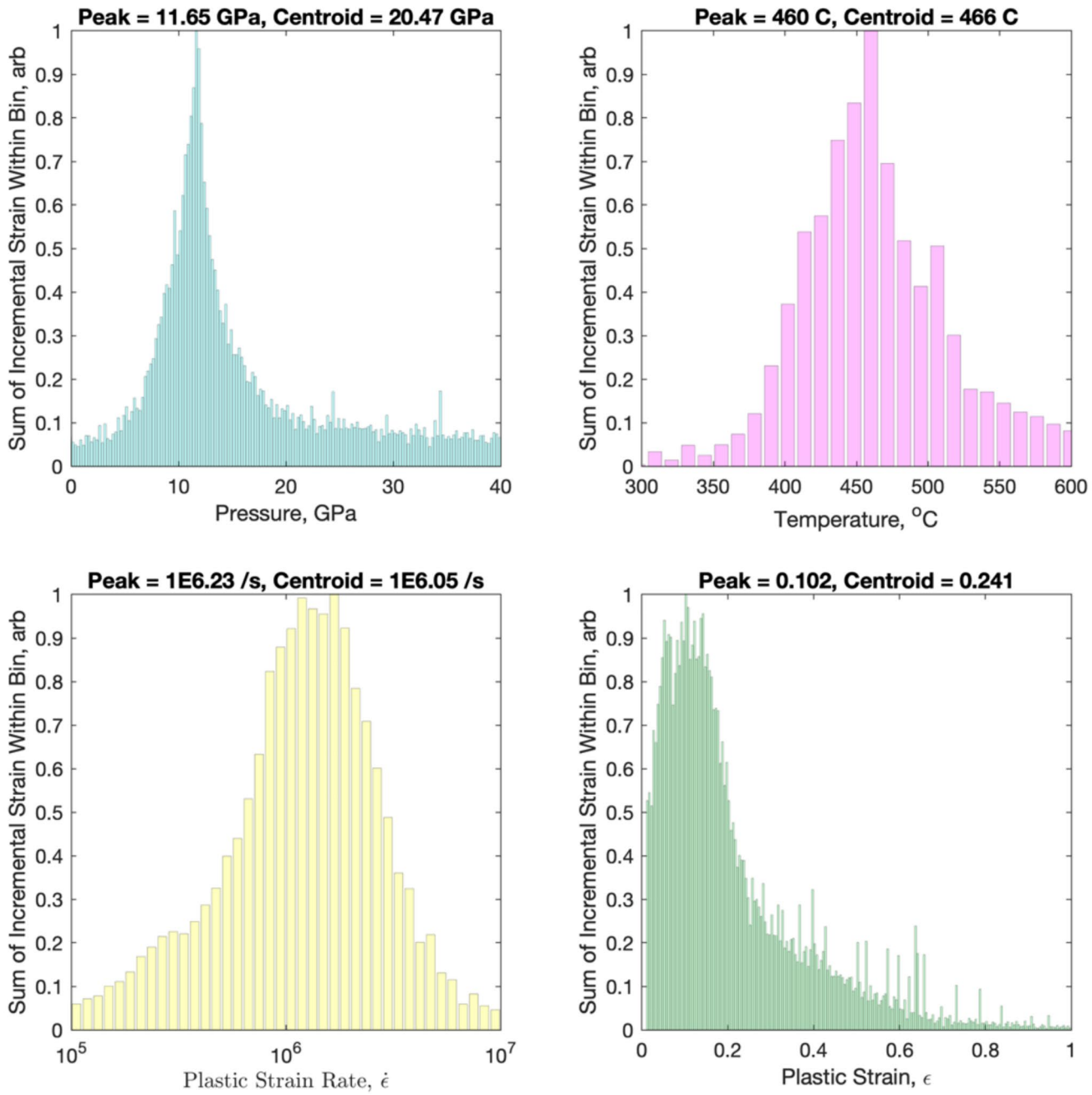

Fig. 15 Histograms of accumulated incremental strain as a function of loading pressure, temperature, strain rate, and strain for shot 22–4-035

accumulated instantaneous strain vs. pressure, temperature, and strain rate are generated for each experiment. This methodology is influenced and inspired by the recent Physical Regime Sensitivity work by Dyer [37], but uses a different approach. The data for these histograms are generated through CTH simulations, in which a dense grid of Lagrangian tracers are placed in the Mo driver along the central wavelength, at depths ranging 0.025 to 0.975 mm. These tracers are placed with approximately equal 25 μm spacing, populating 41 tracers along the sinewave at 39 depths, totaling 1599 tracers. A visualization of these tracers applied to simulations of Shot 22–4-035 is shown in Fig. 14. These CTH simulations are almost identical to the strength calibration simulations described in the preceding section, with the only difference being that the Mo yield strength

Table 6 Loading states for each experiment, extracted via histograms of summed incremental strain

SHOT ID	Vel. (km/s)	P_{Peak}(GPa)	$P_{Centroid}$(GPa)	T_{Peak}(C)	$T_{Centroid}$(C)	$\dot{\epsilon}_{Peak}$ $\log_{10}$(/s)	$\dot{\epsilon}_{Centroid}$ $\log_{10}$(/s)	ϵ_{Peak}	$\epsilon_{Centroid}$	RD_{Peak}	$RD_{Centroid}$
22–4-025	1.049	3.57	8.18	111	117	5.73	5.74	0.023	0.077	1.012	1.029
22–4-026	1.404	5.78	12.07	169	175	5.83	5.86	0.013	0.105	1.018	1.042
22–4-027	1.456	5.10	10.68	169	191	5.98	5.90	0.048	0.142	1.016	1.037
22–4-028	1.854	8.67	15.76	262	281	6.03	5.95	0.068	0.177	1.028	1.055
22–4-029	2.277	13.92	20.99	564	573	6.18	6.07	0.148	0.239	1.042	1.066
22–4-030	2.223	16.80	24.84	553	545	6.18	6.02	0.063	0.183	1.054	1.078
22–4-035	2.066	11.65	18.77	460	466	6.23	6.05	0.103	0.218	1.035	1.060
22–4-036	2.326	18.57	26.44	611	602	6.18	6.03	0.083	0.206	1.058	1.082
23–2-006	0.769	2.42	6.63	100	159	5.88	5.87	0.023	0.207	1.007	1.023
23–2-007	0.529	1.93	4.78	65	86	5.73	5.67	0.018	0.094	1.014	1.017

The subscripts *Peak* and *Centroid* are descriptive of whether the value is extracted from the peak or centroid of the strain-based histogram

is constrained to be between the jet length calibrated and contour calibrated values, with a uniform distribution.

To generate histograms of loading condition as a function of instantaneous strain, the instantaneous amount of strain at each tracer location is calculated as the product of the plastic strain rate and the time step. This instantaneous strain is then summed in bins of pressure, temperature, strain rate, strain, and relative density to produce histograms, an example is shown in Fig. 15. Histogram outliers are removed using a moving median algorithm. The peak (mode) and centroid (average) of each histogram are used to define the nominal loading conditions associated with the calibrated strength values. Drive stresses and release stresses are calculated via impedance matching and reported alongside calibrated yield strengths in Table 5. Loading states calculated using the strain-based histogram analysis are reported in Table 6. Note that all strain rates fall within a narrow range on a logarithmic scale and could be approximated as nominally 10^5–10^6 /s. Plots of calibrated strengths as a function of loading pressure and temperature are shown in Fig. 16.

The loading states tabulated in Table 5 show that the temperature at which strain occurs is highly correlated with the drive stress, whereas the pressure at which strain occurs is highly correlated with the release stress. This result is expected and follows the trends described in the numerical study by Vogler & Hudspeth [20]. Future experiments that use higher energy radiography can explore higher shock pressures within the same shock temperature range by using higher shock impedance tampers.

Mesh Sensitivity Effects on Strength Calibration

To evaluate the effect of mesh size on the strength calibration process, simulations are performed at 10 mesh element sizes ranging from 2 to 26 μm, with equal spacing. Yield strength is varied from 0.80 to 1.60 GPa in 0.10 GPa increments. The calibrated yield strengths for each methodology are plotted in Fig. 17 as a function of mesh size.

Figure 17 show the effects of mesh size on calibrated yield strengths for the jet length and contour calibration methods. Generally, the jet length comparison method has a larger sensitivity to mesh size than the contour comparison method, meaning the contour comparison method could yield more realistic results at coarser mesh resolutions than the jet length comparison method. From these plots, it can be seen that the calibrated yield strengths using 2 μm mesh element length (500 elements/wavelength) are within 1% of the asymptotic values. This suggests that the 2 μm mesh element length used for strength calibration simulations in this work is appropriate.

Comparison of EPP Model Fits to Steinberg–Guinan-Lund Model

Model parameters for the SGL model and a modified version of the SGL model have been previously calibrated for Mo and reported in Steinberg, [21] and Alexander et al., [23]. The model form described by Steinberg [21] is available in CTH, and can thus be directly compared to the experimental data. For this comparison, one simulation is performed for each experiment using the SGL model described in Steinberg [21] and the same geometry and mesh used in the EPP simulations. To directly compare the SGL model to the experimental data and best fit EPP models, jet lengths for each are plotted in Fig. 18.

The jet length profiles plotted in Fig. 18 show that the SGL model reported in [21] consistently underpredicts jet lengths and thus overpredicts material strength at the loading states of the tamped RMI experiments. The SGL model can provide a better fit to the experimental data by modifying its fitting parameters; however, the SGL model has many fitting parameters and thus the process of iteratively modifying the

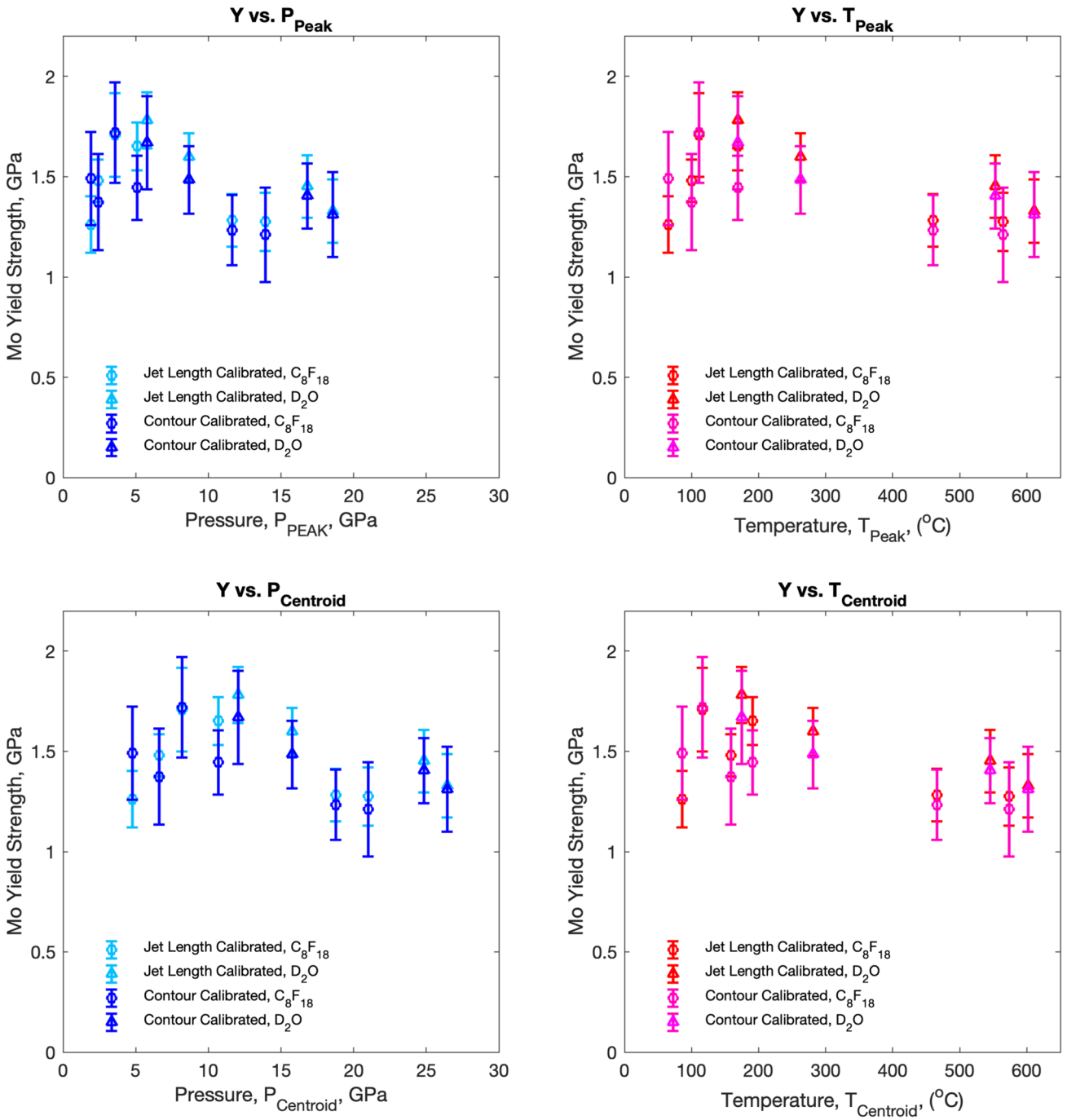

Fig. 16 Calibrated yield strengths as a function of the pressures and temperatures extracted using the strain-based histogram method

SGL parameters to fit the full series of experiments would be cumbersome. This motivates our use of the EPP model to find the average yield strength and average loading state of the Mo in each experiment.

Uncertainty Quantification

Uncertainty in Calibrated Yield Strength

To evaluate the uncertainty in calibrated yield strength values, 1000 simulation iterations are performed for each experiment varying the impact velocity, sinewave geometry

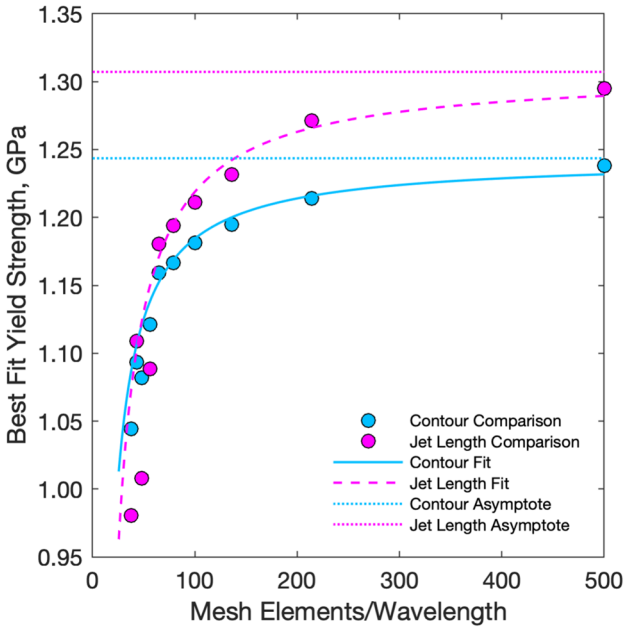

Fig. 17 Best fit yield strength as a function of mesh size for both the contour comparison and jet length comparison methods

(wavelength and amplitude), Mie-Grüneisen EOS parameters for the Mo and tamping fluid (D_2O or C_8F_{18}), and Mo yield strength. These simulations are performed by interfacing CTH with the Sandia code Dakota, using Dakota to populate values each for each uncertain parameter. In this format, maximum/minimum bounds are applied to each parameter and values are selected randomly using Latin hypercube sampling within uniform uncertainty distributions. Impact velocity bounds are defined by the slowest and fastest velocities recorded using the DCS barrel-mounted optical beam breaks. Sinewave wavelengths are varied within 5 μm of the nominal value, approximating the wire EDM machine precision. Sinewave amplitudes are varied by the sinewave misfit error, δ_{SM}, listed in Table 7

The Mie-Grüneisen EOS parameters ρ_0, C_0, S, and C_V are varied by 1, 2, 2, and 5%, respectively, for both the Mo and tamping fluids. The Mie-Grüneisen γ_0 value is varied by 5% for Mo and 20% for both tamping fluids. Lastly, the Mo yield strength is allowed to vary ± 0.5 GPa about the best fit strength value for the specific experiment. To reduce computational overhead, uncertainty quantification simulations are performed with a uniform mesh element length of 10 μm, 100 elements/wavelength and 8.6 million cells per simulation, matching the resolution of tamped RMI sensitivity studies performed by Vogler and Hudspeth [20]. All uncertainty simulations use the same boundary conditions applied during the strength calibration process.

The outputs of these 1000 uncertainty quantification simulations are plotted in Fig. 19 and used to evaluate the calibrated yield strength uncertainty range for each experiment. To determine the mean curve, a moving centroid is calculated using 0.050 GPa yield strength bins, accounting for approximately 50 data points per bin. Deviation distances from each individual point to this centroid curve are calculated, then histograms of these point-to-centroid deviation distances are used to define the standard deviation of the centroid curve. Standard deviations are calculated asymmetrically for the positive and negative deviations. These standard deviations are defined as the 68.27% confidence interval of histograms within 0.05 GPa yield strength bin sizes. Note that this calculation is similar to the edge reproduction uncertainty calculation in Sect. "UncertaintyQuantification for Radiography: Edge Reproduction". Figure 19 shows an example plot of the 1000 uncertainty quantification iteration outputs, centroid curves, and standard deviations for Shot 22–4-035.

Uncertainty in calibrated yield strength is defined as the range of yield strengths within an allowable maximum deviation of contour or jet length, $\epsilon_{max,j,c}$. This maximum deviation is defined by a combination of the edge reproduction uncertainty, δ_{ERU}, sinewave misfit, δ_{SM}, standard deviations of the centroid curve at the best fit strength, $\sigma_{j,c}$, and the remaining deviation at the best fit yield strength, $\delta_{\mathrm{min,j,c}}$, i.e.,

$$\epsilon_{max,j,c} = \delta_{\mathrm{min,j,c}} + \sigma_{j,c} + RSS_{j,c},$$

$$RSS = \sqrt{\delta_{ERU}^2 + \delta_{SM}^2 + \delta_{min,(j,c)}^2},$$

where the subscripts j and c are used to indicate whether the value is calculated for the jet length calibration or contour calibration methods, respectively. Uncertainty in yield strength is thus defined by the range of strength values where the lower standard deviation curve, centroid- $\sigma_{j,c}$, is less than the ϵ_{max} value, as is graphically shown in Fig. 19. This uncertainty range is calculated for each experiment and reported in Table 7.

Discussion

Generally, the Mo dynamic yield strength decreases as the drive stress increases, as shown by the negative trends in Fig. 16. To better understand this trend, a plot of calibrated yield strengths vs. pressure (P_{Peak}) and temperature (T_{Peak}) is shown in Fig. 20. From this plot the compensating effects of thermal softening and pressure hardening can be observed. The two liquid tampers used in this work push the Mo through different trajectories of pressure and temperature

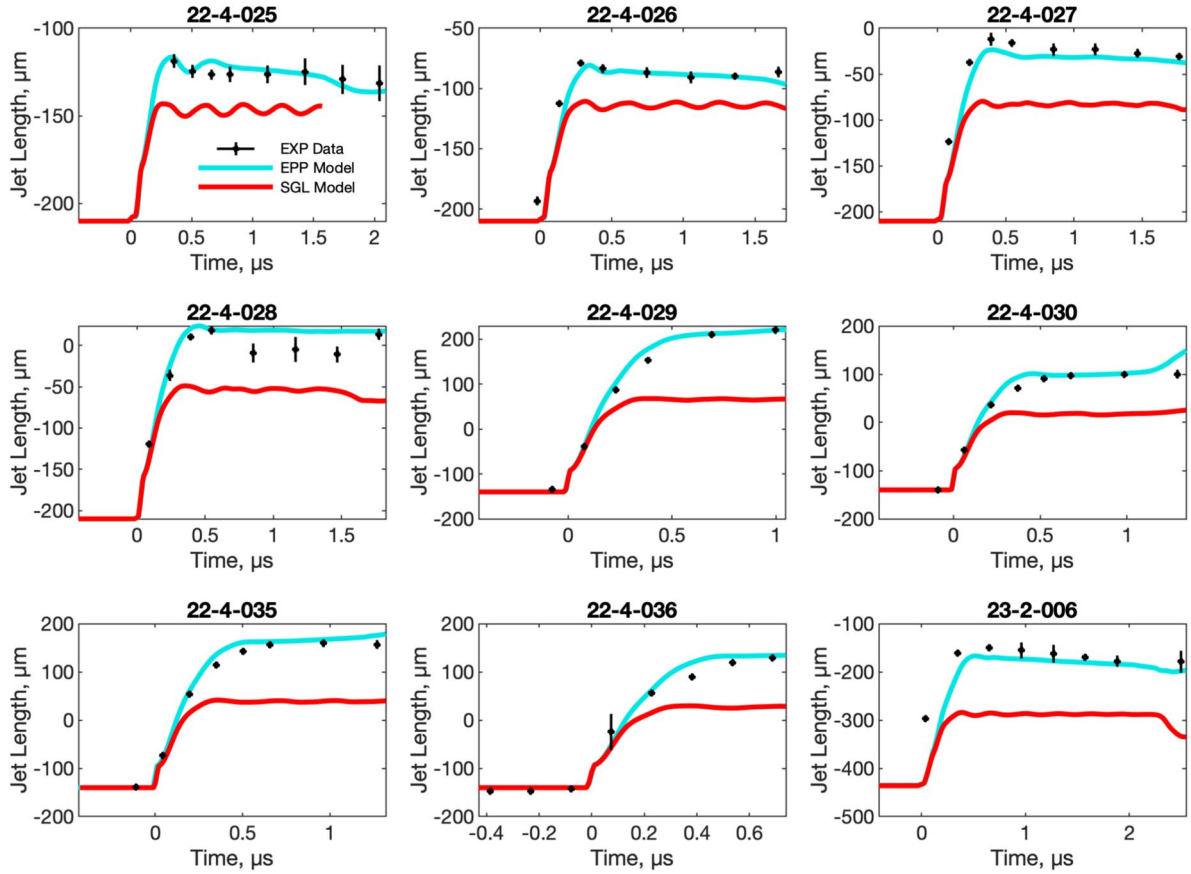

Fig. 18 Comparison of the SGL and best fit EPP models to the experimental jet lengths. Experimental data is shown as black scatter points, the best fit EPP model is shown in cyan, and the SGL model [21] is shown in red. Shot names are shown as plot titles, and experiment 23–2-007 is omitted to reduce plot size

Table 7 Uncertainty values per experiment: edge reproduction uncertainty, δ_{ERU}, sinewave misfit uncertainty, δ_{SM}, minimum of uncertainty centroid, $\delta_{min,C}$ or $\delta_{min,J}$, uncertainty in calibrated yield strength, $\delta Y_{Contour}$ or $\delta Y_{JetLength}$

Shot ID	Frames in ROI	δ_{ERU}(μm)	δ_{SM}(μm)	$\delta_{min,C}$(μm)	$\delta_{min,J}$(μm)	$\delta Y_{Contour}$(±GPa)	$\delta Y_{JetLength}$ (±GPa)
22–4-025	6	2.23	2.13	1.54	5.52	0.25	0.21
22–4-026	4	2.92	1.48	2.18	2.71	0.24	0.14
22–4-027	6	2.84	2.43	3.74	3.97	0.16	0.12
22–4-028	5	3.02	1.58	4.82	4.94	0.17	0.12
22–4-029	2	2.21	1.89	11.50	11.03	0.24	0.17
22–4-030	3	2.52	1.05	2.88	6.12	0.16	0.16
22–4-035	3	2.19	1.04	6.21	8.29	0.18	0.16
22–4-036	2	2.59	2.97	4.59	7.30	0.21	0.18
23–2-006	5	2.93	11.17	7.31	6.27	0.24	0.11
23–2-007	5	2.60	1.23	2.45	8.90	0.23	0.14

space, as the datapoints for the C_8F_{18} tamper are at consistently higher pressures than the D_2O tamper at similar temperatures. Comparing experiments 22–4-028 and 22–4-035, a significant decrease in yield strength occurs as the nominal temperatures increase from 250 to 448 C for nominal pressures near 10 GPa. Comparing experiments 22–4-029 and 22–4-030, a small increase in yield strength occurs as the nominal pressures increase from 12.3 to 16.8 GPa for nominal temperatures near 550 C. Generally, the collection of data in this study suggest that thermal softening has a larger effect than pressure hardening on Mo dynamic yield strength within the physical regimes accessible via tamped

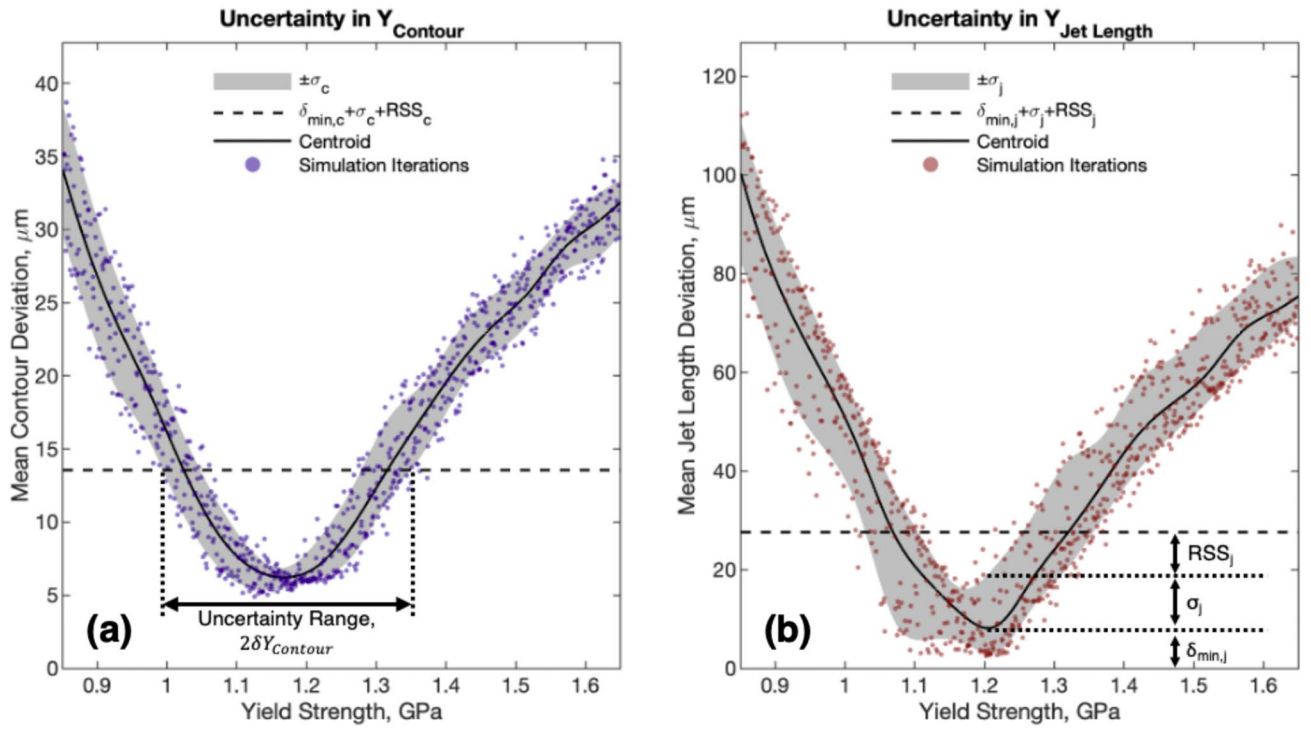

Fig. 19 Visualization of the uncertainty analysis applied to yield strengths calibrated via **a** contour comparison or **b** jet length comparison. Example data are shown for 1000 simulation iterations of Shot 22–4-035, varying the input values described in Sect. "Uncertainty in Calibrated Yield Strength"

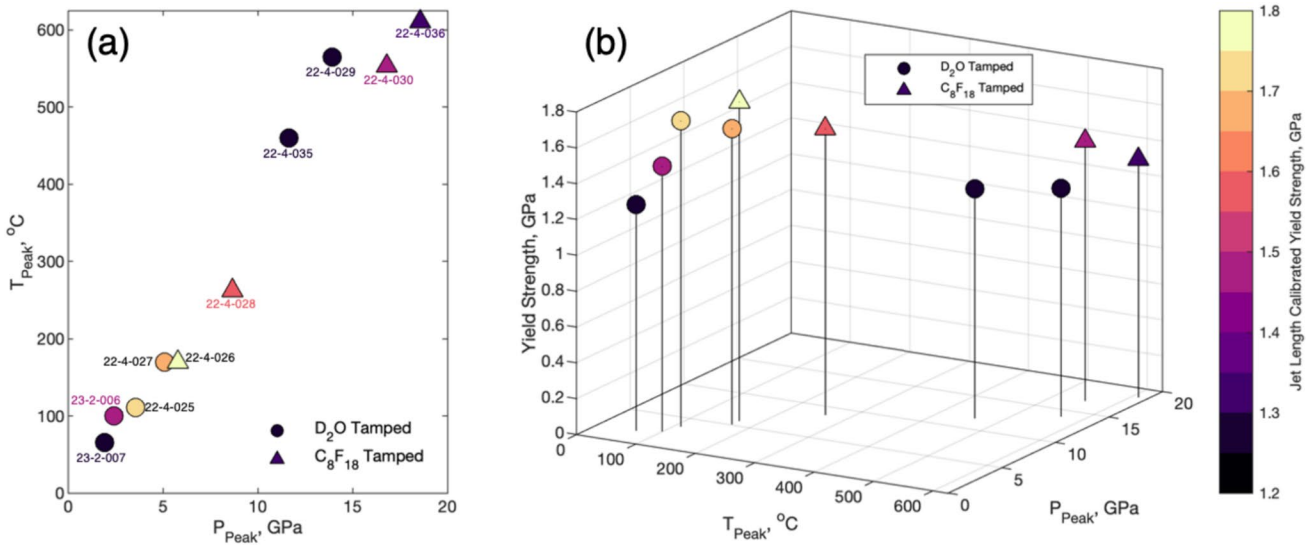

Fig. 20 Dynamic yield strengths of Mo as a function of both temperature and pressure during strain. Yield strengths shown are calibrated using jet lengths. Pressures and temperatures are the peak values in Table 6. **a** Overhead projection with shot numbers labeled. **b** Isometric view

RMI. To further explore the competing behavior of thermal softening and pressure hardening in the ultrahigh strain rate regime, a denser tamping fluid could be used to strain the Mo at a higher pressure and similar temperature to previous experiments.

The decreasing strength trend suggests that Mo exhibits significant thermal softening under dynamic loading conditions. This thermal softening behavior is also observed in the quasistatic-to-intermediate strain rate characterization work performed by Briggs and Campbell [38], and described by Steinberg in [21]. If thermal softening is the primary reason for the observed strength decrease in the present work, then the current work suggests that physical mechanisms governing thermal softening at ambient pressure and quasistatic strain rate conditions persist to strain rates in the 10^6 /s regime. Although these trends in strength vs. loading state strongly suggest thermal softening as the reason for the observed decrease in Mo dynamic yield strength vs. increasing drive stress, the trend could be caused by strain localization or strain softening. Further investigations would be needed to fully distinguish between the effects of thermal softening and strain localization.

Conclusion

This study utilizes and improves upon the tamped RMI method to evaluate the dynamic yield strength of Mo at 3–18 GPa pressures, 50–600 C temperatures, and 4.5×10^5–1.1×10^6 /s strain rates. This study provides multiple improvements to the tamped RMI method, including a dynamic yield strength calibration cost function based on RMI contour shape, the quantification and tabulation of loading states where strain occurs, a robust uncertainty quantification method, and the use of variable density liquid tampers. The contour calibration cost function described in this work can be applied to RMI experiments that do not use sinewave geometries, allowing the use of easier to fabricate geometries in future tamped RMI experiments, such as drilled cavities or milled channels. The tabulation of yield strengths vs. loading conditions presented in this work can be used to fit or develop complex dynamic strength models. The methodologies described in this work can be applied to any future tamped RMI experiments to tabulate strength versus loading state information. These methods may also be applicable to other instability experiments, such as RTI and untamped RMI.

The Mo yield strength values calibrated in this work range 1.2–1.8 GPa, with strength generally decreasing as the drive stress increases. These strength vs. loading state data strongly suggest that this trend is caused by thermal softening, meaning that Mo thermal softens in the shock regime at moderate shock stresses. This suggests that simulations of Mo under shock compression loading and significant shear must appropriately capture thermal softening to accurately predict Mo performance.

Acknowledgements This work was conducted at Sandia National Laboratories and the Dynamic Compression Sector. Special thanks are given to Brian Holliday and Bryant Morgan of Sandia National Laboratories for their support in machining all target components and programming the wire EDM, respectively. Sandia National Laboratories is a multi-mission laboratory managed and operated by National Technology & Engineering Solutions of Sandia, LLC (NTESS), a wholly owned subsidiary of Honeywell International Inc., for the U.S. Department of Energy's National Nuclear Security Administration (DOE/NNSA) under contract DE-NA0003525. This written work is authored by an employee of NTESS. The employee, not NTESS, owns the right, title and interest in and to the written work and is responsible for its contents. Any subjective views or opinions that might be expressed in the written work do not necessarily represent the views of the U.S. Government. The publisher acknowledges that the U.S. Government retains a non-exclusive, paid-up, irrevocable, world-wide license to publish or reproduce the published form of this written work or allow others to do so, for U.S. Government purposes. The DOE will provide public access to results of federally sponsored research in accordance with the DOE Public Access Plan. This publication is based upon work performed at the Dynamic Compression Sector, which is operated by Washington State University under the U.S. Department of Energy (DOE)/National Nuclear Security Administration award no. DE-NA0003957. This research used resources of the Advanced Photon Source, a DOE Office of Science User Facility operated for the DOE Office of Science by Argonne National Laboratory under contract no. DE-AC02-06CH11357.

Funding U.S. Department of Energy.

Declarations

Conflict of interest The authors declare that they have no known competing financial interests or personal relationships that could have appeared to influence the work reported in this article.

References

1. Johnson CR (2021) Micromechanics of additively manufactured materials under dynamic loading. Marquette University
2. Johnson GRC, William H (1983) A constitutive model and data for metals subjected to large strains, high strain rates and high temperatures. In: Proceedings from the 7th International Symposium on Ballistics, The Hague, The Netherlands.

3. Steinberg DJ, Cochran SG, Guinan MW (1980) A constitutive model for metals applicable at high-strain rate. J Appl Phys 51(3):1498–1504. https://doi.org/10.1063/1.327799
4. Steinberg DJ, Lund CM (1989) A constitutive model for strain rates from 10^−4 to 10^6 s−1. J Appl Phys 65(4):1528–1533. https://doi.org/10.1063/1.342968
5. Brown JL, Alexander CS, Asay JR, Vogler TJ, Ding JL (2013) Extracting strength from high pressure ramp-release experiments. J Appl Phys. https://doi.org/10.1063/1.4847535
6. Prime MB, Fensin SJ, Jones DR, Dyer JW, Martinez DT (2024) Multiscale Richtmyer-Meshkov instability experiments to isolate the strain rate dependence of strength. Phys Rev E 109(1–2):015002. https://doi.org/10.1103/PhysRevE.109.015002
7. Grady DE (1988) The spall strength of condensed matter. J Mech Phys Solids 36(3):353–384. https://doi.org/10.1016/0022-5096(88)90015-4
8. Field JE, Walley SM, Proud WG, Goldrein HT, Siviour CR (2004) Review of experimental techniques for high rate deformation and shock studies. Int J Impact Eng 30(7):725–775. https://doi.org/10.1016/j.ijimpeng.2004.03.005
9. Vogler TJ, Chhabildas LC (2006) Strength behavior of materials at high pressures. Int J Impact Eng 33(1–12):812–825. https://doi.org/10.1016/j.ijimpeng.2006.09.069
10. Bakhrakh OB, Kovalev NP, Lebedev AI, Meshkov EE, Mikhailov AL, Nevmerzhitsky NV, Nizovtsev PN, Rayevsky VA, Simonov GP, Solovyev VP, Zhidov IG (1997) Hydrodynamic Instability in Strong Media (UCRL-CR-126710). (Lawrence Livermore National Laboratory Internal Report, Issue. https://www.osti.gov/servlets/purl/515973
11. Buttler WT, Oró DM, Preston DL, Mikaelian KO, Cherne FJ, Hixson RS, Mariam FG, Morris C, Stone JB, Terrones G, Tupa D (2012) Unstable Richtmyer-Meshkov growth of solid and liquid metals in vacuum. J Fluid Mech 703:60–84. https://doi.org/10.1017/jfm.2012.190
12. Dimonte G, Terrones G, Cherne FJ, Germann TC, Dupont V, Kadau K, Buttler WT, Oro DM, Morris C, Preston DL (2011) Use of the Richtmyer-Meshkov instability to infer yield stress at high-energy densities. Phys Rev Lett 107(26):264502. https://doi.org/10.1103/PhysRevLett.107.264502
13. Hudspeth M, Olles J, Mandal A, Williams J, Root S, Vogler T (2020) Strength of porous α-SiO2 in a shock loaded environment: Calibration via Richtmyer-Meshkov instability and validation via Mach lens. J Appl Phys. https://doi.org/10.1063/5.0028026
14. Olles JD, Hudspeth MC, Tilger CF, Vogler TJ (2021) The effect of liquid tamping media on the growth of richtmyer-meshkov instability in copper. J Dyn Behav Mater 7(2):338–351. https://doi.org/10.1007/s40870-021-00305-8
15. Prime MB, Buttler WT, Buechler MA, Denissen NA, Kenamond MA, Mariam FG, Martinez JI, Oró DM, Schmidt DW, Stone JB, Tupa D, Vogan-McNeil W (2017) Estimation of metal strength at very high rates using free-surface richtmyer-meshkov instabilities. J Dyn Beh Mater 3(2):189–202. https://doi.org/10.1007/s40870-017-0103-9
16. Prime MB, Buttler WT, Fensin SJ, Jones DR, Brown JL, King RS, Manzanares R, Martinez DT, Martinez JI, Payton JR, Schmidt DW (2019) Tantalum strength at extreme strain rates from impact-driven Richtmyer-Meshkov instabilities. Phys Rev E 100(5–1):053002. https://doi.org/10.1103/PhysRevE.100.053002
17. Sternberger Z, Opachich Y, Wehrenberg C, Kraus R, Remington B, Alexander N, Randall G, Farrell M, Ravichandran G (2018) Investigation of hydrodynamic instability growth in copper. Int J Mech Sci 149:475–480. https://doi.org/10.1016/j.ijmecsci.2017.08.051
18. Zhou Y (2017) Rayleigh-Taylor and Richtmyer-Meshkov instability induced flow, turbulence, and mixing. I Physics Reports 720–722:1–136. https://doi.org/10.1016/j.physrep.2017.07.005
19. Zhou Y (2017) Rayleigh-taylor and richtmyer-meshkov instability induced flow, turbulence, and mixing II. Phys Rep 723–725:1–160. https://doi.org/10.1016/j.physrep.2017.07.008
20. Vogler TJ, Hudspeth MC (2021) Tamped richtmyer-meshkov instability experiments to probe high-pressure material strength. J Dyn Behav Mater 7(2):262–278. https://doi.org/10.1007/s40870-020-00288-y
21. Steinberg DJ (1993) A rate-dependent constitutive model for molybdenum. J Appl Phys 74(6):3827–3831. https://doi.org/10.1063/1.355316
22. Steinberg DJ (1996) Equation of State and Strength Properties of Selected Materials. Lawrence Livermore National Laboratory, Livermore
23. Alexander CS, Ding JL, Asay JR (2016) Experimental characterization and constitutive modeling of the mechanical behavior of molybdenum under electromagnetically applied compression-shear ramp loading. J Appl Phys. https://doi.org/10.1063/1.4943496
24. Chhabildas LC, Barker LM, Asay JR, Trucano TG (1989) Spall strength measurements on shockloaded refractory metals. Sandia National Lab, SNL-NM, Albuquerque, NM, USA
25. Furnish MDCLC (1991) Dynamic Material Properties of Refractory Metals: Molybdenum. High Strain Rate Behavior of Refractory Metals and Alloys Fall meeting of the Minerals, Metals and Materials Society of AIME and Materials Week of the American Society of Metals, Cincinnati, OH, United States
26. Furnish MD, Chhabildas LC, Steinberg DJ, Gray GT (1992) Dynamic Behavior of Fully Dense Molybdenum. In: Schmidt SC, Dick RD, Forbes JW, Tasker DG (eds) Shock Compression of Condensed Matter–1991. Elsevier
27. Duffy TS, Ahrens TJ (1994) Dynamic response of molybdenum shock compressed at 1400 °C. J Appl Phys 76(2):835–842. https://doi.org/10.1063/1.357758
28. Cotton M, Millett J, Whiteman G, Park N (2012) Spall strength of niobium and molybdenum. AIP Conf Proc 1426(1):1031–1034. https://doi.org/10.1063/1.3686454
29. Kanel GI, Razorenov SV, Utkin AV, Fortov VE, Baumung K, Karow HU, Rusch D, Licht V (1993) Spall strength of molybdenum single crystals. J Appl Phys 74(12):7162–7165. https://doi.org/10.1063/1.355032
30. Scapin M, Peroni L, Carra F (2016) Investigation and mechanical modelling of pure molybdenum at high strain-rate and temperature. J Dyn Beh Mater 2(4):460–475. https://doi.org/10.1007/s40870-016-0081-3
31. WSU (2022) Target Fabrication For Impact Experiments, Dynamic Compression Sector (DCS) (Dynamic Compression Sector User Guide, Issue. W. S. University. https://dcs-aps.wsu.edu/documents/2022/01/impact-target-assembly-user-manual.pdf/
32. Jensen BJ, Cherne FJ, Prime MB, Fezzaa K, Iverson AJ, Carlson CA, Yeager JD, Ramos KJ, Hooks DE, Cooley JC, Dimonte G (2015) Jet formation in cerium metal to examine material strength. J Appl Phys. https://doi.org/10.1063/1.4935879
33. Ruggirello KCT (2023) CTH User's Manual, Version 13.0.
34. Voorhees T, Vogler T (2025) SAND2025–07596C: Validation of using the elastic-perfectly plastic model to calibrate and tabulate average dynamic yield strength and loading conditions in impact-driven tamped Richtmyer-Meshkov instability experiments. In: 24th International Conference on the Science of Compression in Condensed Matter, Washington, D.C., USA.
35. Guo S, Voorhees TJ, Sapp AW, Vogler TJ (2023) Optical Response and Hugoniot State of Shock-compressed Perfluorooctane. Sandia National Lab, SNL-NM, Albuquerque, NM, USA
36. GMX-6 G (1969) Selected Hugoniots.

37. Dyer JW, Waters J, Prime MB (2024) Robust implementation of Physical Regime Sensitivity and demonstration on Richtmyer-Meshkov Instability experiments. J Mech Phys Solids. https://doi.org/10.1016/j.jmps.2024.105656
38. Briggs TL, Campbell JD (1972) The effect of strain rate and temperature on the yield and flow of polycrystalline niobium and molybdenum. Acta Metall 20(5):711–724. https://doi.org/10.1016/0001-6160(72)90100-9